Effect of Polymer Confinement: Tuning Self-Assembled Growth of Monodisperse Au Nanoparticles on Polystyrene Films

Sudeshna Chattopadhyay and Alokmay Datta*

Surface Physics Division, Saha Institute of Nuclear Physics, 1/AF, Bidhannagar, Kolkata 700 064, India

Received October 19, 2006; Revised Manuscript Received February 2, 2007

ABSTRACT: X-ray reflectivity and tapping mode atomic force microscopy reveal that, Au, sputter-deposited on polystyrene films for film thickness $\leq 4R_g$ (R_g being unperturbed polymer gyration radius), diffuse and coalesce slowly, under ambient conditions and predominantly along the polymer surface, to form nanoparticles. The nanoparticles are highly monodisperse, and their in-plane dimensions increase with decrease in polystyrene film thickness. The observed directed coalescence is caused by sharply defined, higher surface energy zones or "traps", corresponding to lower cohesion, between gyration spheres on polystyrene film surface. Lowering of in-plane cohesion and coalescence are found only when gyration spheres are layered along film depth due to thinning of the polystyrene film. The coalescing potential of these traps is given by the spatially localized increase in surface energy and can be increased by confinement. This fact is the principle behind this tunable self-assembly—a new and generalized mode of self-assembly of Au nanoparticles with monodispersity and tunability in size.

Introduction

Polymers have the unique property that their molecular dimensions can be in the nanometric length scales. Of course, what "molecular dimensions" of a polymer mean has to be qualified. If we consider the polymer in the state of maximum entropy as regards the orientations of monomers, we obtain the polymer molecule in a spherical conformation,[1] the so-called "gyration sphere", with its dimension given by radius of gyration $R_g = 0.272M^{1/2}$, where M is the molecular weight of the polymer.[2] Nanometer sized gyration spheres of almost any polymer are thus observed[2−4] if a sufficiently high order of polymerization is achieved.

In the past decade a large number of experimental observations have established that fluids, when confined to films supported on substrates, form molecular layers parallel to the substrate surface.[5−7] It has been shown that complex fluids such as colloids and polymers[8,9] also can be nanoconfined to form such layers where the layer period corresponds to some molecular size: the colloid dimension or the radius of gyration. More relevant to our discussion here are the recent findings that, at least for polystyrene, the cohesion between these layers are reduced with respect to bulk.[10] This reduction is initiated when polystyrene film thickness is reduced to $4R_g$ and, while the value of the reduction in cohesion is constant for a particular film thickness, it increases with decrease in film thickness. The diffusion of materials,[11] including self-diffusion,[12] as well as transfer of energy,[10] across polymer film thickness is again found to be drastically reduced with respect to bulk, as these layers are formed. This reduction of cohesion along film thickness is expected to have some significant effect on the distribution of free energy on polymer film surface and, as we have pointed out in the previous paragraph, an understanding of this may provide a means to control surface diffusion of material in the nanometric scale. The reproducible reduction of cohesion, along thickness, of a nanoconfined polymer and its variation with polymer film thickness suggests a generalized means of achieving *tunable self-assembly* of nanoparticles, i.e., tunability of nanoparticle size and shape while retaining monodispersity, perhaps the most important goal in nanomaterials research, via the effects of such reduction on free energy distribution on this polymer film surface and its consequences on surface diffusion of deposited materials.

In this paper, we have presented a realization of tunable self-assembly using a nanoconfined polymer as the template for self-assembled growth of nanoparticles. Specifically, we have shown that Au, sputter-deposited on a spin-coated polystyrene (PS) film on fused quartz forms initially a thin layer, and then, under ambient conditions and over a period of 2 months, diffuses[13] and coalesces to form monodisperse nanoparticles on the film surface. The in-plane dimensions of these nanoparticles increase on solely decreasing the thickness of the PS film, i.e., the degree of confinement of the PS substrate and *not* the duration of the initial Au deposition. In particular, only below a critical PS film thickness ($4R_g$), this coalescence can take place. We have found that, formation of layers with period $\sim R_g$, for polystyrene thickness $\leq 4R_g$ and the consequent decrease in out-of-plane cohesive energy[10] creates sharply defined surface energy variations with fixed dimensions on PS film surface. Trapping the initially diffusing Au in these higher free energy regions forms nanoparticles with fixed size and shape. The strength of these "traps" increases with decrease in film thickness.

The organization of the article is as follows. In the Experimental Section, we have outlined the process of sample preparation, the techniques of data collection through grazing incidence X-ray reflectivity (GIXR) and tapping mode atomic force microscopy (TM-AFM), and the analysis schema used for extraction of electron density profiles (EDPs) along film thickness from X-ray data and extraction of surface energy maps of pristine PS films from AFM phase images. In the next section, we first present the results of nanoparticles formation and show that (a) these particles are highly monodisperse, (b) their shapes and sizes depend only on the thickness of the PS film on which they form, and (c) their shapes and sizes do not depend on the deposition parameters like dosage (the other parameters are kept constant). We then show how the formation of nanoparticles is correlated to the formation of layers in the PS films due to confinement, i.e., thinning the film below a certain thickness,

---

* Corresponding author. Telephone: 91-033-2337-5345, Ext 4216. Fax: 91-033-2337-4637. E-mail: alokmay.data@saha.ac.in.

10.1021/ma0624088 CCC: $37.00

and present the surface energy maps to exhibit the emergence of sharply defined maxima (traps) in these maps as the layers are formed. In the final section we draw our conclusions about this new mode of nanoparticle growth.

Experimental Section

Polystyrene (mol wt $M \approx 560900$ g mol^{-1}, unperturbed radius of gyration ≈ 20.4 nm)[2] was spin-coated onto polished fused quartz (Qtz) substrates (10 mm × 10 mm × 1 mm) from 5.5 to 15.0 mg mL^{-1} toluene solutions, at angular velocities varying from 1.00 to 4.00 krpm, using a photo resist spin-coater (Headway Inc.), to prepare films of thickness varying from $\sim 2R_g$ to $\sim 8R_g$, which correspond to 40−160 nm. The quartz substrates were cleaned according to the RCA cleaning procedure using ammonia and hydrogen peroxide solutions, followed by rinsing in acetone and ethyl alcohol. A series of these PS films was used as the pristine (pPS) samples while Au was sputter-coated on a second identical series forming the AuPS samples. Au was sputtered on PS films of different thickness by a dc magnetron coater (Pfeiffer) always under identical conditions and with the same dose to prepare one set of AuPS films. Deposition was for 10 s at 25 W, 10 sccm Ar gas flow, under 4.7×10^{-3} mbar pressure (base pressure $= 8.6 \times 10^{-6}$ mbar). Another set was prepared by using PS films of same thickness but different deposition times (10, 15, and 25 s) of Au. Stopping and Range of Ions in Matter (SRIM) calculations[14] show that Au is deposited with a mean energy ≤ 2 eV, about an order of magnitude less than the bond strengths in PS, precluding any chance of polymer damage due to Au deposition. No further processing of the samples was carried out and all samples were studied under ambient conditions.

Grazing incidence X-ray reflectivity data of pPS and AuPS films with $R_g \leq d \leq 8Rg$ were collected using an 18 kW rotating anode X-ray generator (Enraf Nonius FR591). The Cu Kα_1 line at $\lambda = 0.1540562$ nm was selected with a Si(111) monochromator and measurements were carried out in a triple-axis diffractometer (Optix Microcontrole). Specular reflectivity scans, i.e., scans in the plane containing the incident beam and the normal to the sample surface, with incident angle α_{in} = scattering angle α_{sc}, were performed with α_{in} varying from 0° to 3° in 5 mdeg steps. If $\boldsymbol{q} = \boldsymbol{k_s} - \boldsymbol{k_i}$ is the momentum transfer vector with $\boldsymbol{k_{s(i)}}$ being the scattered (incident) X-ray wave vector, then this geometry makes the components in the sample plane, $q_x = q_y = 0$, and the value of q_z ($= (4\pi/\lambda) \sin \alpha_{in}$), the component normal to the sample surface, vary from 0 to 4.3 nm^{-1}. The resolution in q_z is $\cong 2.9 \times 10^{-3}$ nm^{-1} and the spatial resolution along film depth is given by $2\pi/q_z^{max}$ where q_z^{max} is the maximum value of q_z for which Kiessig fringes are observed. In our experiments, this gives a typical value of $\cong 1.5$ nm for z resolution. We have measured the off-specular background in all the samples. This was found to be about one-third of the specularly scattered intensity at the maximum q_z (0.3 Å^{-1}) used. This off-specular background profile was subtracted from the specular profile and this background-subtracted data has been analyzed. We have analyzed our reflectivity data using two different schemes.

The reflectivity data of AuPS films are analyzed by the (more general) Parratt formalism. This scheme recursively solves Fresnel equations at each interface, i.e., change in electron density (ρ) within any film. More precisely, in this method, we recursively solve the equation for the reflectance $r_{n-1,n}$ at the interface between the nth and the $(n - 1)$th layers, with the nth layer having thickness d_n and electron density ρ_n, given as[15]

$$r_{n-1,n} = \left\{ \frac{(r_{n,n+1} + F_{n-1,n})}{(1 + r_{n,n+1}F_{n-1,n})} \right\} \exp(-iq_{z,n-1}d_{n-1}) \tag{1}$$

where

$$F_{n-1,n} = \frac{(q_{z,n-1} - q_{z,n})}{(q_{z,n-1} + q_{z,n})} \tag{2}$$

with

$$q_{z,n} = (q_{z,0}^{\ 2} - q_{c,n}^{\ 2})^{1/2} \tag{3}$$

$q_{z,0} = q_z$ the z component (normal to surface) of momentum transfer in vacuum or air and $q_{c,n}^{\ 2} = 16\pi\rho_n r_e$ is the critical value of q_z for total external reflection for the nth layer. The constant r_e is the classical electron radius ($=2.8 \times 10^{-6}$ nm). Equation 1 then yields the reflectivity as

$$\mathbf{R}_{n-1,n} = |r_{n-1,n}|^2 \tag{4}$$

This expression for reflectivity, valid for an ideally smooth interface, is modified in presence of the Gaussian interface width ($\sigma_{n-1,n}$) as

$$\mathbf{R}^{\text{rough}}(q_z) = \mathbf{R}(q_z) \exp(-q_z^{\ 2}\sigma^2) \tag{5}$$

We have used the thicknesses d_{Au}, d_{PS}, the electron densities ρ_{Au}, ρ_{PS} for the Au and PS layers and the widths or "roughness" σ_{Au}, σ_{Au-PS}, and σ_{PS-Qtz} for the air/Au, Au/PS, and PS/Qtz interfaces, respectively, as the fit parameters and with the values extracted from the best fit of reflectivity data using eqs 1− 5, have constructed the electron density profiles (EDPs) i.e., the electron density as a function of film depth from the top for AuPS films, after convoluting the profile with the interface widths. The calculated reflectivity profile has also been convoluted by a Gaussian resolution function with a fwhm corresponding to the 400 μm wide detector slit.

The scheme of distorted wave Born approximation (DWBA),[15] which treats the film as a perturbing potential causing the scattering, is very sensitive to small density variations, and has been used to detect density variations due to layering in liquids or polymers.[5,8] Variations of ρ are expected to be small in pPS films and, following our previous studies, we have used the DWBA method to extract EDPs for these films and to look for layer formation. In the DWBA scheme we consider the film to be composed of a number of slices of equal thickness with electron density $\rho(z) = \rho_0 + \Delta\rho(z)$, where $\Delta\rho$ varies with slices but is constant in a slice. The specular reflectivity is then given by[15]

$$\mathbf{R}(q_z) = |ir_0(q_z) + (4\pi r_e/q_z)\,[a_t^{\ 2}(q_z)\Delta\rho(q_z) + a_r^{\ 2}(q_z)\Delta\rho^*(q_z)]|^2 \tag{6}$$

where r_0 is the specular reflectance coefficient of the average film of electron density ρ_0, a_t and a_r are the coefficients for transmitted and reflected amplitudes of the average film, and $\Delta\rho(q_z)$ is the Fourier transform of $\Delta\rho(z)$. By selecting an appropriate number of slices (of width always greater than 1.5 nm, the maximum achievable resolution) and proper ρ_0 for the film, we fit eq 6, after convolution of the calculated reflectivity for the detector slit, to the data for pPS films, keeping $\Delta\rho$'s and air/PS and PS/Qtz Gaussian interface widths (σ_{PS} and σ_{PS-Qtz}) as the fit parameters. The EDP is constructed from the values of $\rho(z)$ obtained from the best fit. The veracity of this procedure has been crosschecked by generating the reflectivity profiles from the extracted EDPs using the Parratt scheme.

AFM images were acquired with Nanoscope IV, Veeco Instruments, using etched Si tip (radius ≈ 10 nm) and phosphorus-doped Si cantilevers. We have worked in the tapping mode with A_0, the free amplitude of the cantilever = 36 nm, A, the set point amplitude = 10.94 nm, ω_0, the resonance frequency $= 2\pi \times 283$ kHz, Q, the quality factor = 505, and k, the cantilever spring constant = 20 N/m. Both topographic and phase images have been collected by us for pPS and AuPS samples. We have estimated the average energy, E_D, dissipated per cycle by the tip over the film surfaces, from the phase images, using the expression[16]

$$\sin\phi = \left(\frac{\omega}{\omega_0}\frac{A}{A_0}\right) + \frac{QE_D}{\pi kAA_0} \tag{7}$$

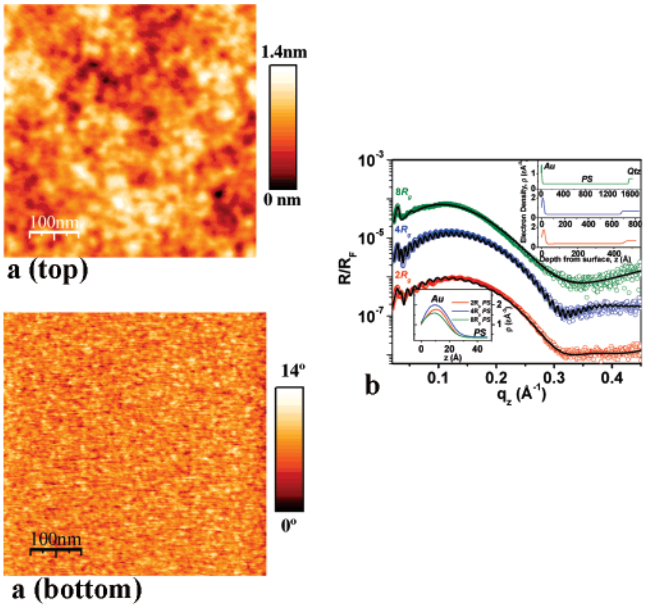

Figure 1. AuPS films immediately after sputter deposition of Au on polystyrene (PS) films. (a) Tapping mode atomic force microscopy (TM-AFM) 500nm × 500 nm scan. Topographic image (top) and phase image (bottom) of PS film with thickness $R \approx 2R_g$. (b) Fresnel normalized X-ray reflectivity (**R/R**$_F$, data in open circles) of typical AuPS films with $R \approx 2R_g$, $4R_g$ and $8R_g$. Corresponding best fits using Parratt method in line. Top inset: electron density profiles (EDPs) across film depth, extracted from fits. Corresponding R is given beside each profile. Reflectivity profiles were up-shifted for clarity. Qtz signifies fused quartz substrate. Bottom inset: Magnified portion of EDP showing Au layers.

where ϕ is the phase-shift with respect to the drive signal and ω is the working frequency. Tip interaction (during approach and retraction) with surface via the van der Waals force is modeled as a sphere approaching a plane with an effective contact area $4\pi r_c \alpha_{Si}$, where r_c is the radius of tip curvature and α_{Si} is the Si atomic diameter. Then relative energy dissipation by the tip in film planes with respect to minima is given by[2,17]

$$\Delta E_D = \frac{2}{3}\frac{r_c \alpha_{Si}}{z_0^2}\Delta A_{SiPS} \qquad (8)$$

where we have considered the tip–sample adhesion, given by the corresponding Hamaker constant A_{SiPS}, to be the varying interaction.[17] This is unaffected by cantilever tilt.[18] Here z_0 is the tip–sample separation ($\approx$ 0.2 nm in contact[2]), $r_c \approx 10$ nm and $\alpha_{Si} = 0.22$ nm. Variation in PS Hamaker constant in the film plane, ΔA_H, can be determined using $A_{SiPS} = A_{Si}^{1/2} A_H^{1/2}$, eqs 7 and 8, and the value of A_{Si}, the Si Hamaker constant.[19] Hence $\Delta\gamma_{PS}$ (in mJ m^{-2}) $\approx \Delta A_H$ (in J)/(2.1 × 10^{-21}), the variation in surface energy, is determined.[2]

Results and Discussion

1. Au Nanoparticles: Tuning of Self-Assembly. The behavior of Au on PS films of different thickness, immediately after sputter deposition for 10 s under identical conditions, is summarized in Figure 1. Parts a and b of Figure 1 show, respectively, the topographic and phase images obtained from tapping mode atomic force microscopy (AFM) and the X-ray reflectivity and EDP of these AuPS films. Figure 1a (top) shows the topographic image while Figure 1a (bottom) shows the phase image of sputter deposited Au on a PS film of thickness $R \approx 2R_g$. Both, in particular the phase image, show an uniform and smooth film with no pronounced morphological features. The same results were obtained irrespective of PS thickness and hence other films with different thickness are not shown. X-ray reflectivity (data in open circles) of films with $R \approx 2R_g$, $4R_g$, and $8R_g$ with the corresponding best fits using Parratt method (in line), has been shown from bottom to top, respectively, in Figure 1b while the EDPs across film depth, extracted from these fits, are shown inset in the same sequence as the reflectivity profiles. The reflectivity profiles have been normalized by Fresnel reflectivity (**R**$_F \propto q_z^{-4}$). The EDPs clearly shows an Au layer of thickness $\cong$ 3 nm on top of PS with no diffusion into the polymer in all cases with coverage ~ 40% - 45%, as calculated from electron density of bulk Au (= 4.391 ϵ Å^{-3}). From these data we find a uniform layer of Au with thickness $\cong$ 3 nm and with similar partial coverage just after sputter deposition (Table 1). The air–Au and Au–PS interfaces are sharp. This indicates negligible diffusion of Au in PS due to the sputter deposition process, in the as-deposited films.

Table 1. Dependence of Au–Nanoparticle Dimensions on Polystyrene (PS) Film Thickness (Measurements on AuPS Films)

	Au nanoparticle dimensions (nm)							
				after 2 months				
	as deposited from X-ray reflectivity			from AFM		from X-ray reflectivity		
PS film thickness[b]	c	σ_{air-Au}	σ_{Au-PS}	a ($\approx b$)	a_d[a]	c	σ_{air-Au}	σ_{Au-PS}
2	3	0.7	0.5	26	25	6	0.7	1.5
3	3	0.9	0.6	21	20	6	0.7	1.5
4	3	0.5	0.6	10	9	6	0.7	1.5
8	3	0.9	0.7			6	0.7	1.5

[a] After deconvolution of the tip effect. [b] In units of R_g, the gyration radius $\approx$ 20.4 nm.

Figure 2 summarizes the condition of the above AuPS films after 2 months of keeping in desiccators at room temperature and under identical conditions. The topographic (top) and phase (bottom) images in Figure 2, parts a–d, corresponding to $R \approx 2R_g$, $3R_g$, $4R_g$, and $8R_g$, respectively, show the presence of nanoparticles with circular in-plane cross-section, with decreasing values of the in-plane dimensions, a and b ($a \approx b$) as PS thickness (R) is increased and finally, for the thickest PS film, no such particle is seen to be formed. Characteristic reflectivity profiles for $R \approx 2R_g$, $4R_g$, and $8R_g$ are shown (open circles for data, lines for best fits), again from bottom to top, in Figure 2e and EDPs, extracted from these fits, are shown in the same sequence inset. From the EDPs it is seen that the out-of-plane dimension, c, has grown to about 6 nm in 2 months but has remained invariant with PS film thickness. Though in all cases there is the same growth along depth yet, interestingly, for the cases of in-plane coalescence the EDPs show a lower density region ("hole") in the PS just below Au pointing to an extra Au–PS segregation during coalescence. These results are summarized in Table 1, along with best-fit values of the interfacial widths. The increase in σ_{AuPS} is consistent with Au coalescence. After this, even after passage of 6 months, there is no change in these dimensions, suggesting that growth of the particles has stopped. From Table 1, it is clear that the initial sputter-deposited Au is diffusing and coalescing, predominantly in plane and at room temperature, to form larger nanoparticles with $a \approx b > c$. Such an instance of Au coalescence at ambient temperature, as far as our knowledge goes, has not been reported previously. It is also clear that such in-plane coalescence takes place only when the PS film thickness $R \leq 4R_g$, and that the in-plane size of coalesced nanoparticles increases as R is decreased below this limit. As both Figure 2 and Table 1 show, the coalesced nanoparticles are *largest for the thinnest PS film*, indicating also a stronger driving force for in-plane coalescence. It should be mentioned here that we have minimized the effect

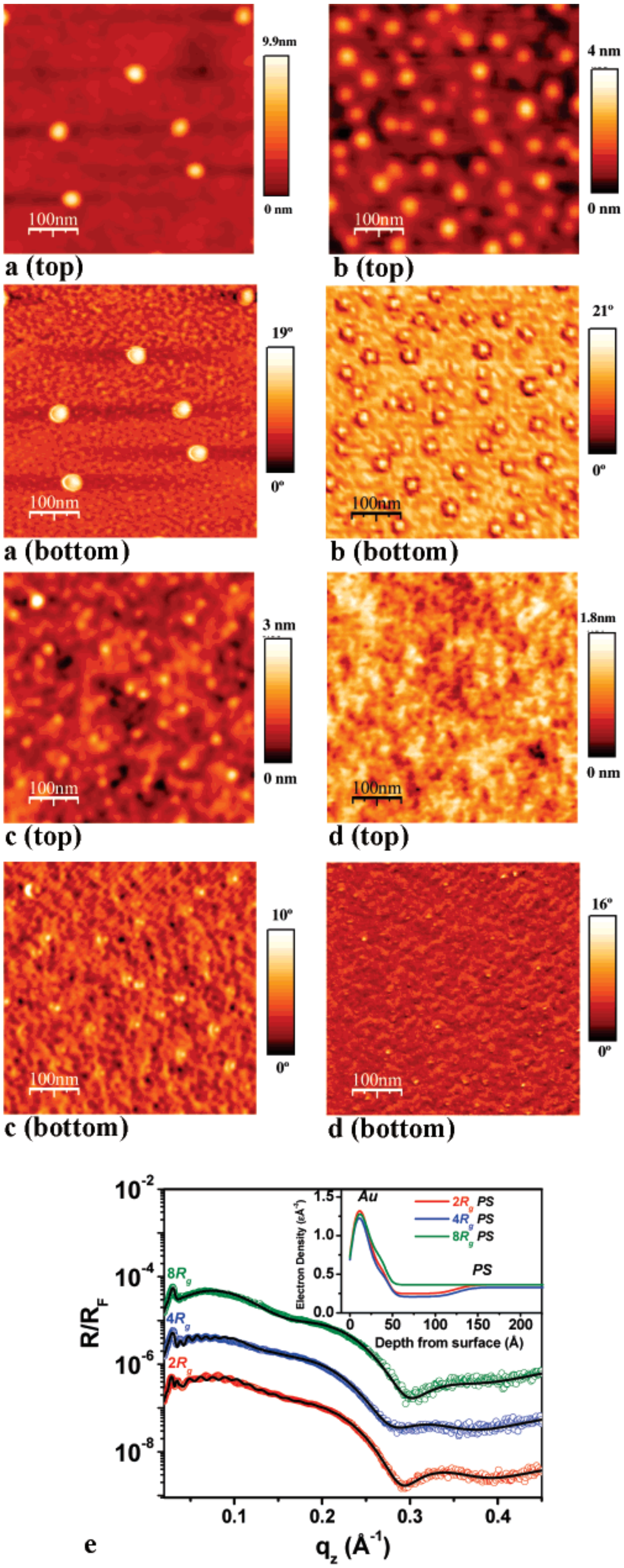

Figure 2. AuPS films 2 months after sputter deposition of Au on PS films. TM-AFM 500nm × 500 nm scans. Topographic (top) and phase (bottom) images for $R \approx 2R_g$ (a), $3R_g$ (b), $4R_g$ (c), and $8R_g$ (d). (e) Fresnel normalized X-ray reflectivity (data in open circles) of films with $R \approx 2R_g$, $4R_g$ and $8R_g$ with corresponding best fits (in line) using Parratt method. Inset: EDPs across film depth, extracted from fits. Corresponding R is given beside each profile. Reflectivity profiles arbitrarily up-shifted for clarity.

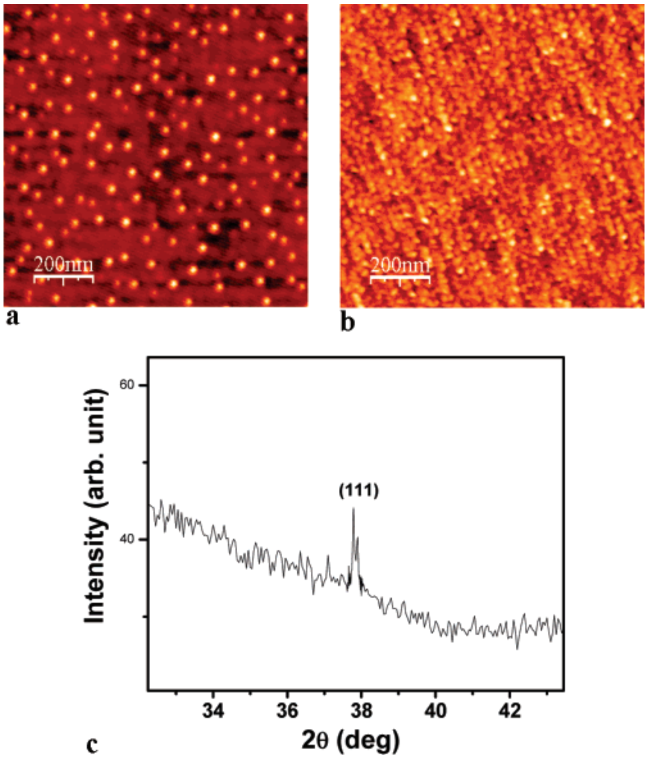

Figure 3. Effects of Au sputter deposition time on AuPS films. TM-AFM 1 μm × 1 μm topographic images for films with 15 (a) and 25 s (b) sputtering of Au, respectively. $R \approx 4R_g$. (c) X-ray diffraction result of sample b, showing the strongest peak (corresponding to Au(111)).

of convolution by the AFM tip on nanoparticle size measurements by Fourier transformation of the topographic images and the (assumed) spherical tip with radius 10 nm, division of the former by the latter and inverse transformation of the result, using Mathematica (version 5). The deconvoluted dimension (a_d) has been presented in Table 1.

To investigate the effect of duration of Au sputter deposition on the morphology of the coalesced nanoparticles, we compared AuPS films, with fixed PS film thickness, on which Au was sputtered for 10, 15, and 25 s and kept under identical conditions (in desiccators under ambient temperature) for 2 months. Figure 3 depicts the characteristic results for PS films with $R \approx 4R_g$. Figure 3a and Figure 3b show the topographic images of AuPS films with 15 and 25 s sputtering of Au. It is clear that increasing the duration of Au deposition only increases number density of the coalesced nanoparticles and not their dimensions. Thus, the size and shape of these nanoparticles are tuned primarily by the *thickness* of the polymer film on which the metal is sputter-deposited. Independence of coalesced particle morphology on initial Au coverage is in contrast to results obtained in general with physical vapor deposition processes[20] and indicates the presence of spatially localized free energy extrema characteristic of self-assembly processes.[17,21] X-ray diffraction measurements (using Cu Kα radiation in a Versatile X-ray diffractometer, Bruker-Nonius) on the AuPS film with $R \approx 2R_g$ and deposition time of 25 s show only one prominent peak at $\theta = 18.9°$ (Kα_1 at 18.895°, Kα_2 at 18.95°; Figure 3c), which corresponds to Au(111). Very weak peaks corresponding to Au(200) and Au(220) were also observed, consistent with results on nanocrystalline Au.[22]

This characteristic is reinforced by Figure 4, which presents the monodispersity of coalesced nanoparticles. Figures 4a and 4b show, respectively, topographic and phase images of Au-

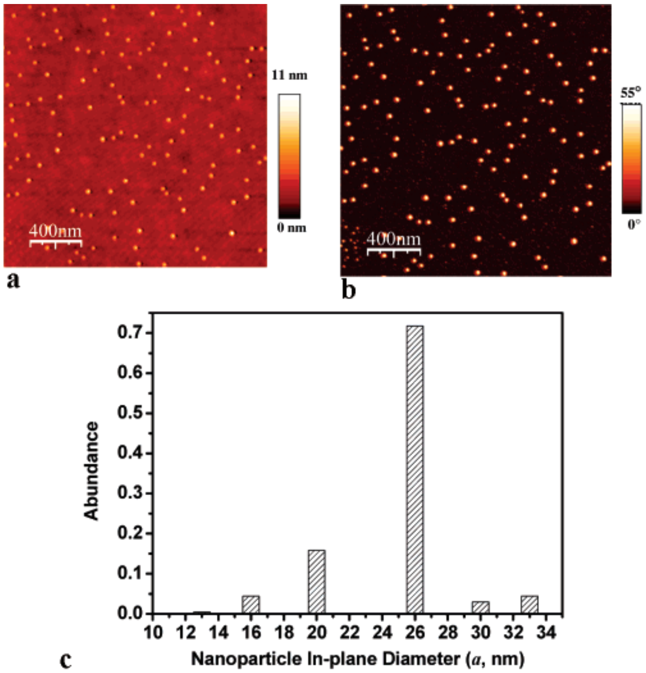

Figure 4. Monodispersity in Au nanoparticle size. (a) Topographic and (b) Phase images of 2 μm × 2 μm TM-AFM scans of Au nanoparticles formed on $2R_g$ thick *PS* film 2 months after Au deposition. (c) Histogram of in-plane size distribution of Au nanoparticles of corresponding film (abundance vs *a* plot (in filled circles), a ($\approx b$) is the in-plane dimension of nanoparticles in parts a and b).

nanoparticles formed on the $2R_g$ thick PS film 2 months after deposition, while Figure 4c presents, in bar graph, abundance of nanoparticles with a particular value of a ($\approx b$) as a function of a. We have averaged the abundance over four 2 μm × 2 μm scans, involving 202 particles. The mean value of a, from this distribution is 26 nm with a standard deviation $\sigma = 1.2$ nm (4.6%). This distribution is completely different from the lognormal distribution of sizes of nanoparticles formed by random coalescence[23] in that there is a sharp upper cutoff in nanoparticle size, consistent with the observation in Figure 3 and very similar to that seen in colloid formation.[24] However, the size distribution seen here is much sharper than those in lognormal distribution or colloid growth. The monodispersity observed here has been found to be undisturbed for $R \leq 4R_g$. This size-selective growth precludes any random coalescence mechanism such as the Vollmer–Weber growth,[25] and it strongly suggests a directed mechanism for nanoparticle formation that, however, depends on the polymer film thickness underneath.

2. The Growth Mechanism. T_G, the glass transition temperature of bulk PS ($\approx$ 100 °C),[26] or even its surface ($\approx$ 77 °C),[26] is well above room temperature. The fact that Au is still diffusing on the PS surface, albeit slowly, to cause the observed coalescence, indicates low Au–PS adhesion.[13,27] Therefore, two-dimensional Brownian motion is a possible mechanism of diffusion.[13] It is also known that, near T_G, there is a "liquid-like" surface layer of thickness ~ 4 nm for polymers in general[28] on which surface diffusion of clusters has been found to be orders of magnitude faster than bulk diffusion.[25] We assume that a two-dimensional Brownian motion, even at ambient conditions, is taking place for the initially deposited Au. This constitutes the first "driving force" for room-temperature coalescence and growth of nanoparticles. However, as we have discussed in the previous subsection, there is a clear indication of a stronger, directed force for coalescence that is superposed on this Brownian motion. We now look at the corresponding pPS films for clues regarding this directed force.

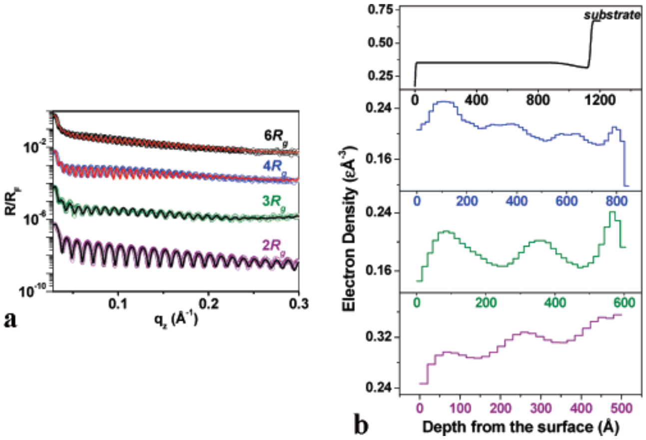

Figure 5. Layering in pristine or pPS films. (a) Fresnel normalized X-ray reflectivity (data in open circles) of films with $R \approx 2R_g$, $3R_g$, $4R_g$ and $6R_g$, with corresponding best fits (in line) using DWBA method. (b) EDPs across film depth, extracted from fits. Corresponding R is given beside each profile. Reflectivity profiles arbitrarily up-shifted for clarity.

Figure 5a shows the reflectivity profiles of pPS films of $R \approx 2R_g$, $3R_g$, $4R_g$, and $6R_g$ from bottom to top respectively. In each case open circles show the reflectivity data while the calculated best fit using the DWBA scheme is shown by solid line and the extracted EDPs are shown in Figure 5b in the same sequence and same color code as reflectivity profiles. Here also the reflectivity profiles have been normalized by Fresnel reflectivity. It is clear from the EDPs that below $d \approx 4R_g$, PS forms layers along film thickness with periodicity $\sim R_g$, suggesting that these layers consist PS molecules in the form of gyration spheres. This phenomenon has been observed previously[9,10] and is depicted here in the cartoon in Figure 6i (left). The key point to note in the present case is that this layer formation is strongly correlated with surface coalescence of Au into nanoparticles, i.e., coalescence takes place only when there is layering. Above the thickness of $4R_g$ layering is absent[10] and there is no variation in EDP for pPS films with thickness $6R_g$ and above (EDPs of such thicker films are therefore not shown). Under ambient conditions, these films were found to be stable against dewetting.

How does layer formation along film depth give rise to directed coalescence or self-assembly along film surface? The answer to this question is in Figure 6. Figure 6a shows the topographical TM-AFM image of a typical pPS film with $R \approx 4R_g$. The topographical images of all these films look the same, having roughly spherical features with an average diameter of R_g shown here.[10] This clearly indicates the presence of gyration spheres in pPS films at all thickness with a size modification.[3] The frusta of these spheres ($\approx$0.6 nm high) are consistent with the top roughness obtained from X-ray studies and presented in Table 2.

Parts b–d of Figure 6 show the TM-AFM phase images of three characteristic pPS films with $R \approx 2R_g$, $4R_g$ and $8R_g$, respectively. In contrast to topographical images, the phase images exhibit larger variations in phase-shifts between adjacent "spheres" on film surface as the thickness is reduced from $4R_g$ to $2R_g$, implying a larger change in energy being dissipated by the AFM tip in going over from one sphere to another.[29] We have calculated $\Delta\gamma_{PS}(x, y)$, the in-plane variation in polymer surface energy for all the pPS films, as outlined in the previous section on experimental details, directly from the phase images. In Figure 6, parts e–g, we have plotted $\Delta\gamma_{PS}(x, y)$ derived from

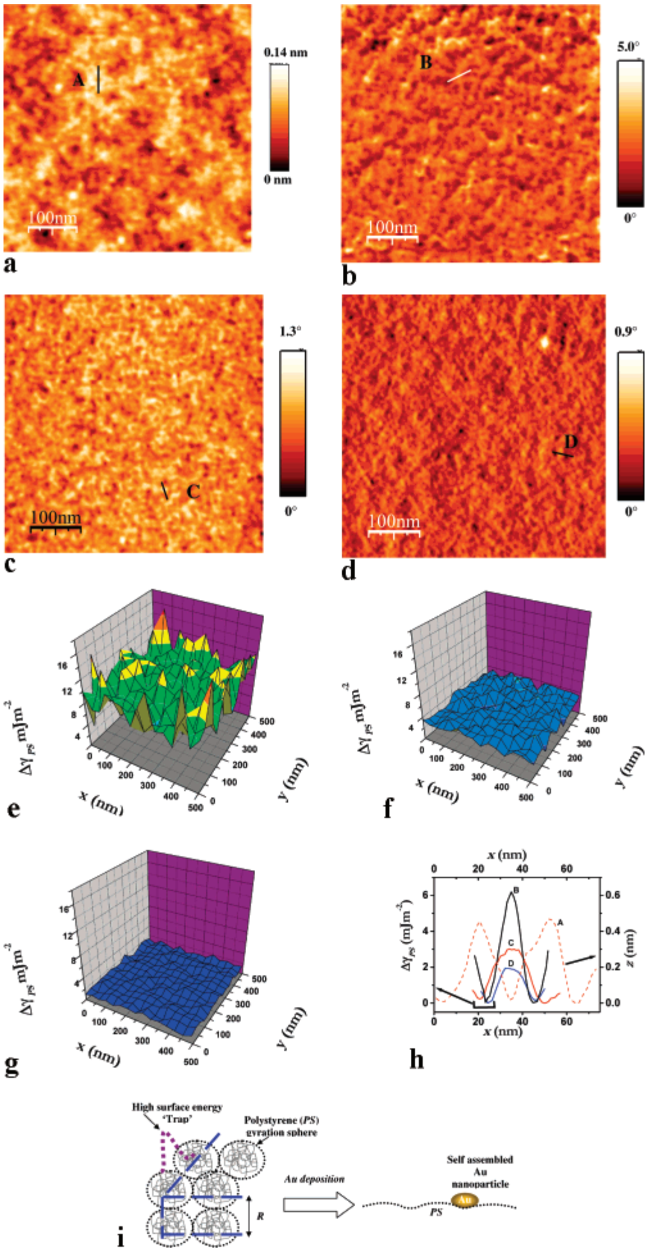

Figure 6. Surface energy landscapes in pPS films. (a) TM-AFM 500nm × 500 nm scan topographic image for films with R ≈ 4Rg. (b−d) TM-AFM phase images for films with $R \approx 2R_g$, $4R_g$, and $8R_g$, respectively. (e−g) In-plane maps of $\Delta\gamma_{PS}$, surface energy relative to top of the gyration spheres for these films (refer text for details). (h) $\Delta\gamma_{PS}$, plotted along typical lines in parts b−d, across adjacent gyration spheres given by curves black, red, and blue, respectively. Topographic profile across line in part a is shown in dashed line. (i) Cartoons showing (left) gyration spheres in a confined polystyrene film and (right) a coalesced Au nanoparticle sitting on the film.

Table 2. Dependence of Polystyrene (PS) Interface Widths and Hamaker Constant Variation on PS Thickness (Measurements on pPS Films)

	interfacial width (nm)[a]		Hamaker constant variation	
PS film thickness	σ_{air-PS}	σ_{PS-qz}	in-plane (ΔA_H,[b] meV)	interlayer (ΔA_H,[c] meV)
2	0.6	0.5	84	97
3	0.3	0.5	45	44
4	0.4	0.5	38	28
6	0.4	0.7	25	∼0

[a] From X-ray reflectivity [b] From AFM phase measurements [c] From ref 10.

Figure 6, parts b−d, respectively, where the length scale of variation is over adjacent gyration spheres and measurements are relative to the sphere tops. Magnitude of $\Delta\gamma_{PS}$, the surface energy variation at the junction of two adjacent gyration spheres relative to the top of the sphere, increases as film thickness reduces from $8R_g$ to $2R_g$ as shown by typical line profiles across such variations superposed on a topographic line profile obtained from Figure 6a (in dashed line) (Figure 6h). Corresponding values of ΔA_H are given in Table 2. They match values of the decrease in Hamaker constant between PS molecular layers, formed by confinement along depth, in films of the corresponding thickness,[10] also presented in Table 2. Thus, confinement lowers cohesion between adjacent gyration spheres, i.e., molecules of PS, both parallel and perpendicular to the direction of confinement as depicted in the cartoon (Figure 6i, left). It is also apparent, from Figure 6, parts e−g, and Table 2, that as film thickness is decreased, i.e., confinement of the polystyrene molecules is increased, the reduction in the cohesion between the gyration spheres is increased, or in other words, the sharp enhancement of surface energy between adjacent spheres is increased. Again, from Figure 2 and Tables 1 and 2, it is apparent that as the enhancement in surface energy between spheres increases the coalesced nanoparticles increase in size while, below a certain level of surface energy enhancement, there is stopping of coalescence. This suggests that the driving forces of the coalescence come from the sharply defined in-plane variations in surface energy. The situation is shown schematically in Figure 6i (right).

The sharp lowering of cohesion between adjacent PS gyration spheres that we observe here indicates a molecular mechanism being involved. Chemical changes are very unlikely during thinning of PS or sputtering of Au. This and our knowledge that thinning breaks intermolecular benzene−benzene noncovalent bonds, specifically resonance transfer interaction between adjacent benzene transition dipoles,[10] lead us to suggest that lowering of cohesion on PS surface is associated with a similar breakdown of inter-benzene connections between adjacent molecular gyration spheres and a possible molecular rearrangement on the sphere tops. The observed lowering of Au−PS adhesion seems also to indicate such a molecular rearrangement.

Conclusion

We have developed a new kind of self-assembled growth of Au nanoparticles utilizing the spatial variations in surface energy in polystyrene films caused by nanoconfinement of the polymer. This is a substrate-directed slow coalescence, under ambient conditions, to monodisperse nanoparticles from an initial layer of Au sputter deposited on the polymer film surface. The coalescence is predominantly two-dimensional, confined to the surface of the polystyrene film, thereby resulting in Au nanoparticles with pronounced in-plane/out-of-plane aspect ratios. Decreasing the underlying polystyrene film thickness can enhance this aspect ratio and size of the nanoparticles, while increasing the polymer film thickness can eventually stop the process of coalescence. We have also seen that the monodispersity and tunability in nanoparticle in-plane dimensions remains unaffected by initial duration of Au deposition, allowing for a larger yield of nanoparticles without loss of the attractive features. We have shown that this growth is correlated strongly to the formation of layers in the polymer film, parallel to the substrate surface, with period nearly equal to the polystyrene gyration radius. This layer formation, which is known to lower cohesion along polymer film thickness, is found to cause lowering of cohesion between adjacent molecular gyration spheres on polystyrene film surface. These low cohesion regions are tantamount to spatially localized high free energy regions whose strength can be tuned by changing the film thickness. These then act as “traps” with tunable strength for coalescence of the sputter deposited Au to assemble into monodisperse nanoparticles, whose in-plane size can be tuned by the strength of the “traps”.

The confinement-induced tuning of such traps, described above, is more generalized than any chemical control of surface energy[30] since there is no change in surface composition. It is known that template-directed assembly maybe achieved by controlling the growth kinetics via spatial distribution of free energy rather than through any epitaxy between the template and the assembled structure,[31] thus already reducing the specificity of the growth process. Our method is a further generalization of this class of template-directed assembly where the template can itself be tuned by simple geometric confinement and is ostensibly applicable to semiconductor and oxide nanoparticles and even to organics. However, besides altering the surface diffusion, such confinement-induced redistribution of surface energy in the polymer is expected to change its thermal, mechanical, optical, and other physicochemical properties that may be interesting for technology as well as basic science. An immediate extension of this work would be to use PS of other molecular weights, since the (out-of-plane) reduction in cohesion has been observed to depend on molecular weight[10] and a dependence of dimensions of nanoparticles assembled on the polymer molecular weight would extend the parameter space for tunability of self-assembly. Another field of interest would be the evolution of crystallinity in the nanoparticle as a function of time, polymer film thickness and molecular weight. Work on these lines are underway.

Acknowledgment. We would like to express our gratitude to Mr. P. Misra, Prof. D. Ghose of our Division, and Mr. J. Tedesco of Veeco Instruments, for their kind cooperation in atomic force microscopy, and Prof. A. Sharma of Indian Institute of Technology for illuminating discussions.

Note Added after ASAP Publication. This article was published ASAP on April 7, 2007. A change has been made to equation 5. The correct version was published on April 18, 2007.

References and Notes

(1) Doi, M.; Edwards, S. F. *The Theory of polymer dynamics*; Clarendon Press: Oxford, U.K., 1986.
(2) Israelachvili, J. N. *Intermolecular and Surface Forces*; Academic Press: New York, 1992.
(3) Kraus, J.; Müller-Buschbaum, P.; Kuhlmann, T.; Schubert, D. W.; Stamm, M. *Europhys. Lett.* **2000**, *49*, 210.
(4) Russell, T. P.; Lambooy, P.; Barker, J. G.; Gallagher, P.; Satija, S. K.; Kellogg, J. G.; Mayes, A. M. *Macromolecules* **1995**, *28*, 787.
(5) Yu, C. J.; Richter, A. G.; Datta, A.; Durbin, M. K.; Dutta, P. *Phys. Rev. Lett.* **1999**, *82*, 2326.
(6) Donnelly, S. E.; Birtcher, R. C.; Allen, C. W.; Morrison, I.; Furuya, K.; Song, M.; Mitsuishi, K.; Dahmen, U. *Science* **2002**, *296*, 507.
(7) Seeck, O. H.; et al. *Europhys. Lett.* **2002**, *60*, 376.
(8) Zwanenburg, M. J.; Bongaerts, J. H. H.; Peters, J. F.; Riese, D. O.; van der Veen, J. F. *Phys. Rev. Lett.* **2000**, *85*, 5154.
(9) Sanyal, M. K.; Basu, J. K.; Datta, A.; Banerjee, S. *Europhys. Lett.* **1996**, *36*, 265.
(10) Chattopadhyay, S.; Datta, A. *Phys. Rev. B.* **2005**, *72*, 155418.
(11) Bhattacharya, M.; Sanyal, M. K.; Chini, T. K.; Chakraborty, P. *Appl. Phys. Lett.* **2006**, 1902. *88*, 7.
(12) Pu, Y.; Rafailovich, M. H.; Sokolov, J.; Gersappe, D.; Peterson, T.; Wu, W. L; Schwarz, S. A. *Phys. Rev. Lett.* **2001**, *87*, 206101.
(13) José-Yacamán, M.; Gutierrez-Wing, C.; Miki, M.; Yang, D. Q.; Piyakis, K. N.; Sacher, E. *J. Phys. Chem. B.* **2005**, *109*, 9703.
(14) www.srim.org.
(15) Sanyal, M. K.; Datta, A.; Hazra, S. *Pure Appl. Chem.* **2002**, *74*, 1553. Basu, J. K.; Sanyal, M. K. *Phys. Rep.* **2002**, *363*, 1.
(16) Tamayo, J.; Garcia, R. *Appl. Phys. Lett.* **1998**, *73*, 2926.
(17) Schirmeisen, A.; Hölscher, H. *Phys. Rev. B.* **2005**, *72*, 45431.
(18) Heim, L.-O.; Kappl, M.; Butt, H.-J. *Langmuir* **2004**, *20*, 2760.
(19) Bollinne, C.; Cuenot, S.; Nysten, B.; Jonas, A. M. *Eur. Phys. J. E* **2003**, *12*, 389.
(20) Welker, T.; Martin, T. P. *J. Chem. Phys.* **1979**, *70*, 5683.
(21) Ikkala, O.; ten Brinke, G. *Science* **2002**, *295*, 2407.
(22) Hazra, S. *Appl. Surf. Sci.* **2006**, *253*, 2154; Šlouf, M.; Kužel, R.; Matěj, Z. *Z. Kristallogr.* **2006**, *Suppl. 23*, 319.
(23) Kunz, M. S.; Shull, K. R.; Kellock, A. J. *J. Appl. Phys.* **1992**, *72*, 4458.
(24) Link, S; El-Sayed, M. A. *J. Phys. Chem. B* **1999**, *103*, 4212.
(25) Narayanan, S.; Lee, D. R.; Guico, R. S.; Sinha, S. K.; Wang, J. *Phys. Rev. Lett.* **2005**, *94*, 145504.
(26) Satomi, N.; Takahara, A.; Kajiyama, T. *Macromolecules* **1999**, *32*, 4474.
(27) Lopes, W. *Phys. Rev. E* **2002**, *65*, 31606.
(28) Sharp, J. S.; Teichroeb, J. H.; Forrest, J. A. *Eur. Phys. J. E* **2004**, *15*, 473.
(29) Tamayo, J.; Garcia, R. *Appl. Phys. Lett.* **1997**, *71*, 2394.
(30) Ryu, D. Y.; Shin, K.; Drockenmuller, E.; Hawker, C. J.; Russell, T. P. *Science* **2005**, *308*, 236.
(31) DiMasi, E.; Olszta, M. J.; Patel, V. M.; Gower, L. B. *Cryst. Eng. Comm.* **2003**, *5*, 346.

MA0624088